Thermally Activated Reverse Electron Transfer Limits Carrier Generation Efficiency in PM6:Y6 Non-Fullerene Organic Solar Cells

Rokas Jasiunas, Huotian Zhang, Andrius Devizis, Marius Franckevicius, Feng Gao and Vidmantas Gulbinas

Jasiunas, R., Zhang, H., Devizis, A., Franckevicius, M., Gao, F., Gulbinas, V., (2022), Thermally Activated Reverse Electron Transfer Limits Carrier Generation Efficiency in PM6:Y6 Non-Fullerene Organic Solar Cells, *Solar RRL*, 6(6), 2100963. https://doi.org/10.1002/solr.202100963

Original publication available at:
https://doi.org/10.1002/solr.202100963

Thermally activated reverse electron transfer limits carrier generation efficiency in PM6:Y6 non-fullerene organic solar cells

Rokas Jasiūnas [1], Huotian Zhang[2], Andrius Devižis[1], Marius Franckevičius[1], Feng Gao[2] and Vidmantas Gulbinas[1]*

[1] Center for Physical Sciences and Technology, Sauletekio av.3, Vilnius, LT-10257, Lithuania
rokas.jasiunas@ftmc.lt

[2] Department of Physics Chemistry and Biology (IFM), Linköping University, Linköping SE-58183, Sweden

Keywords: organic solar cells, non-fullerene, transient absorption, transient photoluminescence, low temperature, PM6, Y6

Abstract Transient absorption and time-resolved fluorescence measurements in a wide temperature range were used to investigate the mechanism of charge carrier generation in efficient organic solar cells based on a PM6:Y6 donor-acceptor blend. The generation mechanisms differ significantly under excitation of a donor or acceptor. The investigations revealed a temperature-dependent interplay between the formation of interfacial charge transfer (CT) states and intra-moiety CT states of the acceptor, their separation into free charge carriers and carrier recombination. The efficient charge carrier generation is ensured by the carrier separation over a small energy barrier, which is easily surmountable at room temperature. However, the overall yield of charge carrier generation at room temperature is reduced by the recombination of charge carriers due to the thermally activated back transfer of electrons from the acceptor to the donor via the HOMO levels, which is enabled by the small energy offset between HOMO levels of the donor and the acceptor.

1. Introduction

Organic photovoltaic (OPV) technology has been gradually developing for few decades[1] and has experienced unprecedented improvement in recent years. The replacement of previously used fullerene derivatives with novel organic molecules known as non-fullerene acceptors (NFAs) has led to state-of-the-art power conversion efficiencies (PCEs) of over 17% in binary bulk heterojunction organic solar cells [2–4]. NFA-based blends exhibit short-circuit currents (J_{sc}) of over 25 mA/cm^2 at standard AM1.5 illumination conditions due to strong acceptor absorption, which is complementary red-shifted compared to a donor [5–8]. Moreover, high J_{sc} values have been demonstrated in NFA systems with remarkably low HOMO energy offsets at the donor-acceptor heterojunctions[9]. Such low carrier generation reaction energies provide low voltage losses, typically slightly above 0.5V [10–12]. Moreover, non-radiative voltage losses are suppressed in NFA-based devices compared to fullerene-based devices, due to the hybridization of the interfacial charge transfer (CT) state with the first excited state, which increases the oscillator strength of the CT state via an intensity borrowing mechanism[10]. In other work, the enhanced radiative decay efficiency in the NFA devices with negligible energy offset has been attributed to stationary-state equilibrium between excitons and CT states[13], suggesting the use of highly luminescent near-infrared emitters for high-efficiency OPV devices.

In 2019 Zou et al. reported a novel non-fullerene acceptor 2,20-((2Z,20Z)-((12,13-bis(2-ethylhexyl)- 3,9-diundecyl-12,13-dihydro-[1,2,5]thiadiazolo [3,4-e]thieno [2,"30′ :4′ ,50]thieno [20,30:4,5]pyrrolo [3,2-g]thieno [20,30:4,5]thieno [3,2-b]indole-2,10-diyl) bis (methanylylidene)) bis(5,6-difluoro-3-oxo-2, 3-dihydro-1H-indene-2,1-diylidene)) dimalononitrile (**Y6**), by employing a ladder-type electron deficient-core-based central fused ring with a benzothiadiazole core [14]. Matched with polymer donor poly[(2,6-(4,8-bis(5-(2-ethylhexyl-3-fluoro) thiophen-2-yl)-benzo [1,2-b:4, 5-b0]dithiophene))-alt-(5,5-(10,30-di-2-thienyl-50,70-bis(2-ethylhexyl) benzo [10,20-c:40,50-c0]dithiophene-4,8‐dione))] (**PM6**), it became one of the best performing material combinations in organic photovoltaics, not only in single-junction, but also in ternary configuration[15,16] and even in upscaled modules[17]. In recent years, several review articles have been devoted solely to the progress of the PM6:Y6 system [18–20]. Although the technical aspects of optimizing PM6:Y6 devices have been extensively covered, there is a clear lack of a comprehensive understanding of the physical basis of charge generation in these materials, which is critical for further improving device performance and developing even better non-fullerene acceptors. For example, two major works [21,22] which scrutinize the photo-physics behind the operation of these PM6:Y6 solar cells reach somewhat different conclusions regarding the role of temperature in electron-hole separation. Wang et al.[21] argue that temperature-assisted charge hopping is involved in charge generation, whereas Perdigón-Toro et al.[22] conclude that the activation energy for dissociation of the CT states is extraordinarily low, at about 6 meV, and therefore photocurrent is efficiently generated down to 100 K. Notably, the studies were limited to 200 K and 75 K lowest temperatures, respectively.

Here we report a detailed investigation of the charge carrier generation mechanism in the PM6:Y6 blend combining transient absorption (TA) and transient photoluminescence (tPL) at various temperatures down to 15 K. The wide temperature range has helped us to uncover previously undiscovered aspects of charge generation in this state-of-the-art photovoltaic material. We show that three distinctly different charge generation pathways coexist: one under excitation of the donor and two under excitation of the acceptor. All of these pathways ensure efficient charge carrier generation at room temperature. However, the final generation efficiency is reduced by the carrier recombination channel opened by the small offset between the HOMO levels of donor PM6 and acceptor Y6.

2. Results

Figure 1 presents the main spectroscopic and electronic properties of PM6 and Y6 materials and their solar cells. The absorption spectra of this donor-acceptor pair ensure efficient absorption of all visible and near IR light and result in a high short-circuit current of over 23 mA/cm^2. A small energy offset between the HOMO levels of the donor and acceptor causes high open-circuit voltage (V_{OC}). The charge carrier generation efficiencies upon light absorption by the donor and the acceptor are comparable, but, as we will show, the generation pathways are very different. We have investigated both pathways through transient absorption studies of the blend films and the pure donor and acceptor films. The blend study was performed with two different excitation wavelengths to ensure a dominant excitation of the donor or the acceptor. Time-resolved photoluminescence spectroscopy was also used to reveal additional details of the charge carrier generation mechanism.

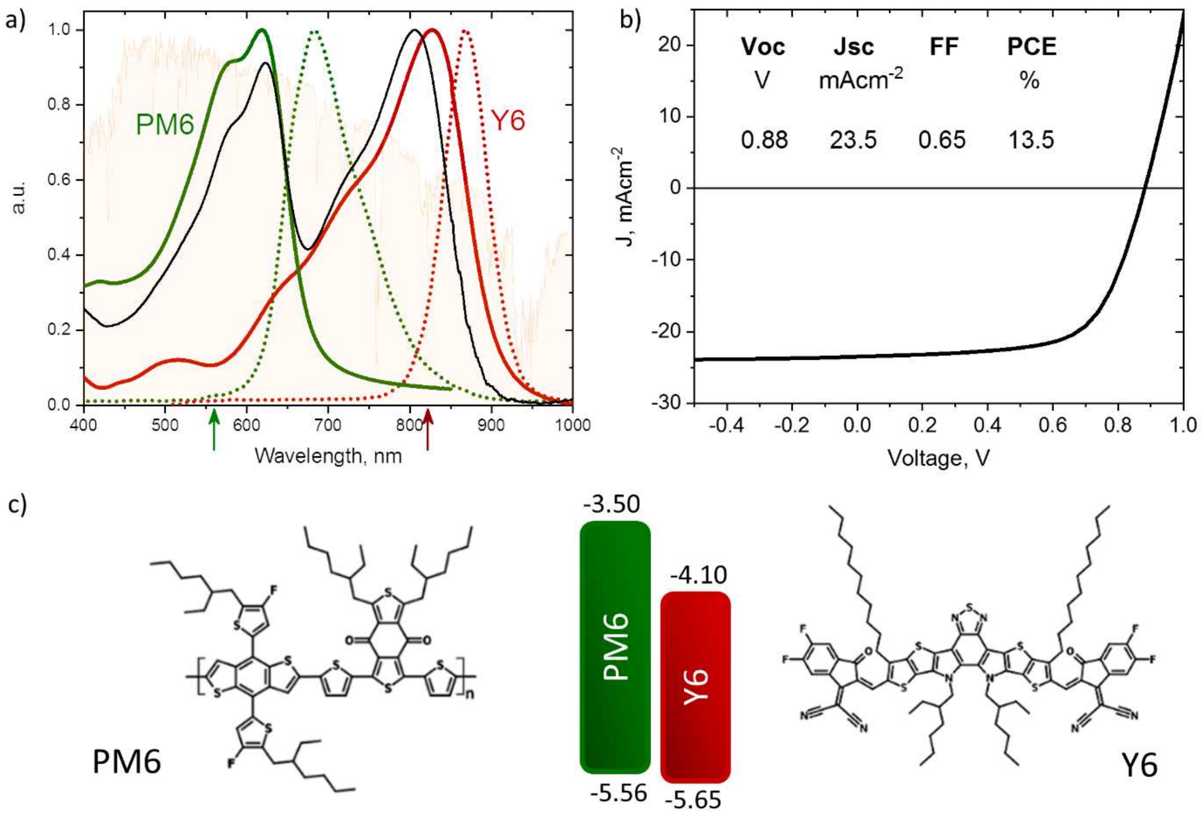

Figure 1. *a) Steady-state absorption spectra of the PM6:Y6 blend (black curve) and the neat PM6 and Y6 films (green and red solid curves) and photoluminescence spectra of the neat films (dashed curves). The light orange curve represents 1.5AM solar irradiation spectrum. The arrows indicate the wavelength used to excite the blend in the TA measurements; b) J-V characteristics of the PM6:Y6 device. c) Chemical structure and energy levels of PM6 and Y6 materials as measured in ref.*[19].

2.1 Transient absorption. Excitation of the donor.

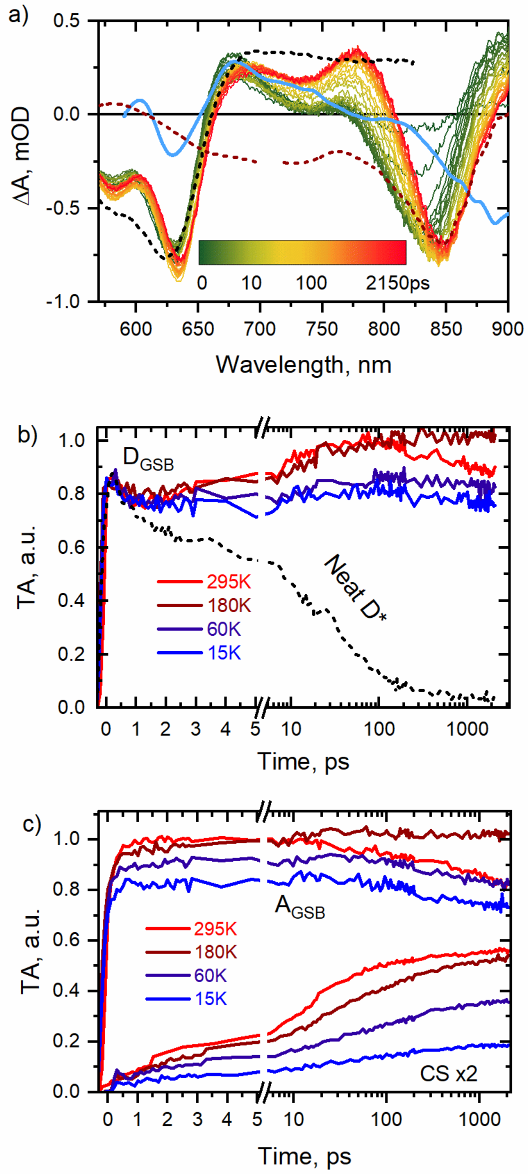

Figure 2. *a) Evolution of the TA spectra of the blend at room temperature after excitation with 560nm laser pulse. The black and brown dashed curves show the normalized TA spectra of donor and acceptor neat films 1ps after excitation with a 560nm or 820nm laser pulse, respectively. The solid light blue curve indicates the electroabsorption spectrum of the blend; b) Kinetics of ground state bleaching of the donor obtained by integrating the TA spectrum in the donor absorption band region (570-650 nm); c) Kinetics of the ground state bleaching of the acceptor, obtained by integrating the TA spectrum in the acceptor absorption band region (770-890 nm), and kinetics of the induced absorption of CS states, obtained by integrating the TA spectrum in the 750-775 nm region.*

To investigate the generation of charge carriers in the PM6:Y6 blend upon excitation of a donor PM6, the donor was preferentially excited with 560 nm light, which is only weakly absorbed by the acceptor (see Fig. 1). Fig. 2a shows the time evolution of the TA spectrum at room temperature (RT). The black and brown dashed lines also show the normalized TA spectra of the pure donor PM6 and pure acceptor Y6 films, which clearly show the ground state absorption bleaching (GSB) bands of the respective materials. TA spectrum of the blend shows the same bleaching bands at 625-650 nm and 820-860 nm corresponding to the GSB of donor PM6 (**D_{GSB}**) and acceptor Y6 (**A_{GSB}**). Fig. 2 b and c show the kinetics of the GSB intensities of the two components at different temperatures. To avoid inaccuracies in the GSB signal dynamics caused by the GSB band shift, the kinetics shown were obtained by integrating the TA signal values in the 570-650 nm range for $\mathbf{D}_{\mathrm{GSB}}$, and in the 770-890 nm range for $\mathbf{A}_{\mathrm{GSB}}$. Next, to avoid possible slight variations in excitation intensity at different temperatures, the kinetics were corrected by normalizing the initial donor absorption bleaching intensity, based on the reasonable assumption that the number of donor molecules initially excited at a fixed excitation intensity is independent of temperature. Excitation of the donor leads to an immediate (within the response time of the device) increase in the $\mathbf{D}_{\mathrm{GSB}}$ signal, while bleaching of the acceptor is slightly delayed (~1ps), which is consistent with the time required for complete electron transfer from the excited donor (**D***) to the acceptor to form an interfacial charge transfer (CT) state or a pair of free charge carriers (referred as CS - charge separated) with holes and electrons located in the donor and acceptor domains, respectively. Thus, both CT and CS states correspond to the ionized donor $\mathbf{D}^{+}$ and acceptor $\mathbf{A}^{-}$. Notably, the strong instantaneous $\mathbf{A}_{\mathrm{GSB}}$ signal component indicates that most electrons are transferred from the excited donor to the acceptor much faster than our time resolution of about 200 fs, which is also typical for fullerene[23–26] and other non-fullerene blends[27–30]. The $\mathbf{A}_{\mathrm{GSB}}$ signal value is slightly lower at reduced temperatures (by ~20% at 15K (Fig. 2c)), indicating that the efficiency of CT state formation decreases slightly at low temperatures. Such a slight decrease is expected because the diffusion lengths of the excitons are shorter at low temperatures and thus the excitons cannot reach the D/A interface.[31] Importantly, the weak temperature dependence shows that the electron transfer involved in the formation of the CT state is a barrierless process, in agreement with the large difference between the LUMO energies of the donor and acceptor (~0.6 eV).

After the immediate appearance, the $\mathbf{D}_{\mathrm{GSB}}$ decreases slightly during the first 1ps, regardless of temperature. This decrease occurs simultaneously with the final development of $\mathbf{A}_{\mathrm{GSB}}$ and, thus probably reflects the difference between TA caused by the **D*** and $\mathbf{D}^{+}$ states. A stronger TA, caused by **D***, is to be expected, as stimulated emission may contribute to TA in addition to

$\mathbf{D}_{\mathrm{GSB}}$. Such a decrease may also be caused by the rapid relaxation of fraction of the **D*** states to the ground state (which is supported by the similar decay rate of a neat donor, dotted curve Fig.1b). Importantly, the discussed decay of the $\mathbf{D}_{\mathrm{GSB}}$ signal was identical at the reduced excitation intensity (see Fig. S2), which ensures that our measurements were performed within the limit of low excitation intensity when the nonlinear intensity-dependent recombination processes can be neglected. After the slight decay, the $\mathbf{D}_{\mathrm{GSB}}$ increases again on a time scale of tens of ps, but this increase is less pronounced at low temperatures. A similar increase was previously reported in ref. [21] and was vaguely attributed to an additional electroabsorption (EA) component that enhances the $\mathbf{D}_{\mathrm{GSB}}$ signal. The EA signal is caused by alternated absorption of unexcited molecules in the presence of induced local electric fields generated by the CT and CS states. The electric field in the CT state is mainly confined between donor and acceptor molecules forming the CT state and therefore has only a weak effect on neighboring molecules. A larger distance between separated charge carriers in CS states leads to expansion of the electric field area. Neutral molecules appear in a strong electric field between and around the charges and enhance the EA spectral signature. Therefore, the EA signal has been used as a probe to track the charge carrier separation dynamics[25,32].

To verify the role of the EA in the formation of the TA spectra and their dynamics in the given blend, we measured the EA spectra induced by an external electric field (Fig.S3). The shape of the EA spectrum with a small kink at ~600 nm, the main $\mathrm{D}_{\mathrm{GSB}}$ band at ~630 nm, and the induced absorption at 675 nm, strongly resembles the measured TA spectra, however, is blue-shifted by about 20 nm. To illustrate this similarity, the light blue curve in Fig. 2a shows the spectrum of EA red-shifted by 20 nm. Such a shift can be caused by different EA formation conditions under macroscopic and local electric fields. The local fields mainly affect molecules that are close to the donor-acceptor interfaces and may have slightly different spectral properties. The local fields may also be much stronger than the applied macroscopic field. Indeed, the measured EA spectrum tends to broaden and red-shift with increasing electric field strength (as shown in Fig. S3), approaching the TA spectrum of the blend. Consequently, our results confirm the hypothesis about the effect of EA on the growth of the $\mathbf{D}_{\mathrm{GSB}}$ signal and, more importantly, provide a tool to probe the dynamics of CT state dissociation to CS state. An alternative approach to probe the dynamics of the formation of CS in the PM6:Y6 blend was proposed in ref.[21], where the authors attributed the 750-790 nm induced absorption band to the absorption of CS states or, more specifically, to the holes in PM6. Though, our data suggest that an attribution to the absorption of holes is rather rash: there are several different constituents in the 750-790 nm range, originating from the **A***, **D***, EA, CT and CS states, therefore this band might be only phantom-like and originate from a changed equilibrium between these constituents during charge separation. Nevertheless, we agree with authors of ref.[21] that the intensity of this band is roughly proportional to the CS state concentration. The dynamics of CS state formation and its temperature dependence, which results from the dynamics of this band intensity, is shown in Fig.1c. On the time scale of 1-100 ps, it closely matches the increasing $\mathbf{D}_{\mathrm{GSB}}$ signal at all temperatures, which is also due to the fact that the CS state formation increases the EA signal.

Although an accurate quantitative assessment of charge separation efficiency based on the spectral features described above is problematic, we can reasonably assume that the CS state formation rate is roughly proportional to the increase rate of these spectral features and therefore apply the Arrhenius formalism to estimate the barrier to the formation of the CS state. The procedure for evaluating CS state formation rate is illustrated in SI Fig. 4S together with the Arrhenius plot obtained. Arrhenius plot deviates strongly from the linear dependence. At 300 K and 180 K we obtain an activation energy of ~14 meV, while at lower temperatures activation energies are lower. Nevertheless, the deduced low activation energy is in reasonable agreement with the value of 6 meV reported in ref.[22]. Such low activation energy was explained by the electrostatic bias potential arising from the large quadrupolar moments of Y6 and the specific acceptor-donor-acceptor molecular architecture that compensates for the Coulomb bonding of the CT state. Our data show that the formation rate of CS states at low temperatures is much larger than predicted by Arrhenius dependence. The 15 K used in our work corresponds to a kT of ~1meV, at which even a marginal barrier of a few meV for the dissociation of the CT state can hardly be overcome. It should be noted that, according to the CS kinetics presented in Fig. 2c, most CS states are generated during a several ps after excitation, especially at 15 K. It hints that CT state dissociation occurs at least in part from non-equilibrated (hot) CT state, similar to what is observed in some fullerene-based solar cells[33–35]. A higher degree of delocalization of the hot CT excitons compared to the relaxed ones increases the probability of charge dissociation[36]. Such hot-state dissociation together with a low activation energy explains the very weak temperature dependence of the CS state formation.

The transient absorption dynamics during 0.1 - 2 ns deserve special attention. The simultaneous decay of donor and acceptor bleaching bands shows that the charge carrier recombination takes place in this time range. Recombination is the most pronounced at RT, but does not occur or is much weaker at 180 K and regains significance at very low temperatures. This process reduces the electron and hole densities by about 10% during 2 ns at RT. The enhanced recombination at very low temperatures can be explained by the fact that large fraction of CT states does not split into CS states. Therefore, CT states eventually recombine by the retransfer of electron from the LUMO of the acceptor to the HOMO of the donor. This process becomes less efficient at higher temperatures, when the CT states split into CS states more rapidly. However, this mechanism also predicts that carrier recombination at RT should be particularly weak when the CT states split very quickly. The rapid recombination at RT therefore suggests that *there is an additional, thermally-activated recombination channel*. Considering a small energy offset of ~100 meV between the HOMO levels of donor and acceptor (as measured in ref.[19]), there could be a thermally-activated reverse electron transfer from HOMO of the acceptor to HOMO of the donor (it may also be considered as a reverse hole transfer), producing the A* state of the acceptor. This channel may also cause recombination of already generated charge carries if they geminately or non-geminately recreate CT states. Since the relaxation of the excited acceptor Y6 (as discussed below) is much faster than the direct recombination (relaxation) of the CT state, this reverse transfer process creates an additional recombination channel activated at RT.

2.2 Excitation of the acceptor.

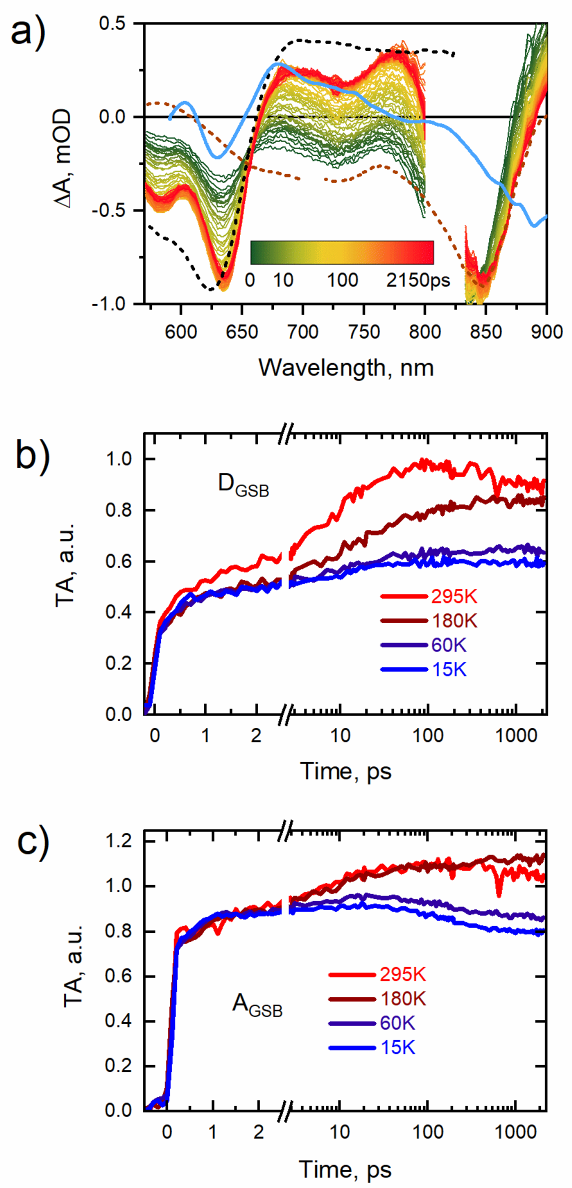

Figure 3. *a) Evolution of the transient absorption spectra of the PM6:Y6 blend after 820nm laser excitation. The black and brown dashed curves show the normalized TA spectra of donor and acceptor neat films 1ns after560nm or 820nm excitation, respectively. The light blue curve shows electroabsorption spectrum; b) Donor ground state bleaching kinetics obtained by integrating the TA spectrum in the donor absorption band region (570-650 nm). c) Acceptor ground state bleaching kinetics, obtained by integrating TA spectrum in the acceptor absorption band region (770-890 nm).*

Let us now examine the path of charge generation by excitation of acceptor Y6. Figure 3a shows the time evolution of the TA spectrum of the PM6:Y6 blend excited at 820 nm at RT. The instantaneous (within experimental resolution) **A**GSB signal is followed by a two-phase **D**GSB signal growth (Fig. 3b and c). The fast phase, which is limited by our time resolution, accounts for about 40% of the total **D**GSB signal at RT. We assign it to conventional direct hole transfer from the excited acceptor (**A***) to the donor, which forms identical interface CT states as in the case of excitation of a donor. The remaining ~60% of the **D**GSB evolves on a timescale of several hundred ps. According to ref.[21], this slow hole transfer channel is mediated via peculiar intra-moiety CT state (xCT) of an acceptor, which forms at RT during ~0.2 ps and dissociates into free polarons within ~15 ps. Our data are consistent with this interpretation. Accordingly, we attribute the slow **D**GSB growth phase to delayed hole transfer from the xCT state or from free electron-hole pairs formed in the acceptor. An additional contribution to the **D**GSB growth may come from the formation of CS states. This process is supported by the delayed (~10ps) appearance of a kink at 570-625nm (Fig.3a) in the TA signal, which is specifically characteristic of EA spectra and absent in the initial **D**GSB signal. However, the contribution of EA can hardly be greater than in the case of donor excitation, resulting in a **D**GSB growth by about 20% at RT. Therefore, most of the growth should still be attributed to delayed hole transfer mediated by xCT states. Importantly, **D**GSB growth slows at low temperatures and is marginal at 15K, indicating that hole transfer mediated by xCT states requires thermal assistance.

The evolution of TA on a timescale of hundreds of ps and a few ns is very similar to that observed under excitation of the donor: We observe a decay of the entire TA spectrum at RT, which disappears at a temperature reduced to 240 K, but is observed again at even lower temperatures. Consequently, both donor and acceptor excitation lead to approximately the same system state during about 100 ps. This state is composed of the CT and CS states, with the ratio depending on the temperature. As with donor excitation, the observed TA decay at room temperature should be attributed to the reverse electron transfer to the donor.

2.3 Transient Photoluminescence

To confirm the above made conclusions and to further elucidate the mechanisms of charge carrier generation, we have performed transient photoluminescence studies with a temporal resolution of less than 5ps. We used an excitation wavelength of 515 nm, which predominantly excites the donor, although weak excitation of the acceptor is also present. It was shown in ref. [37] that the CT state manifold in the PM6:Y6 blend emits only very weakly and is even referred to as dark. Therefore, we can state that PL originates only from neutral excited singlet states of donor and acceptor (**D*** and **A***), so that the intensity of PL unambiguously represents the concentrations of **D*** and **A***. Figure 4a shows the temporally (0-120ps) integrated PL spectra of the blend at different temperatures. Despite the dominant excitation of the donor, the time-integrated PL of the donor is very weak and changes only slightly with temperature, which is in good agreement with the rapid and barrierless formation of interfacial CT states.

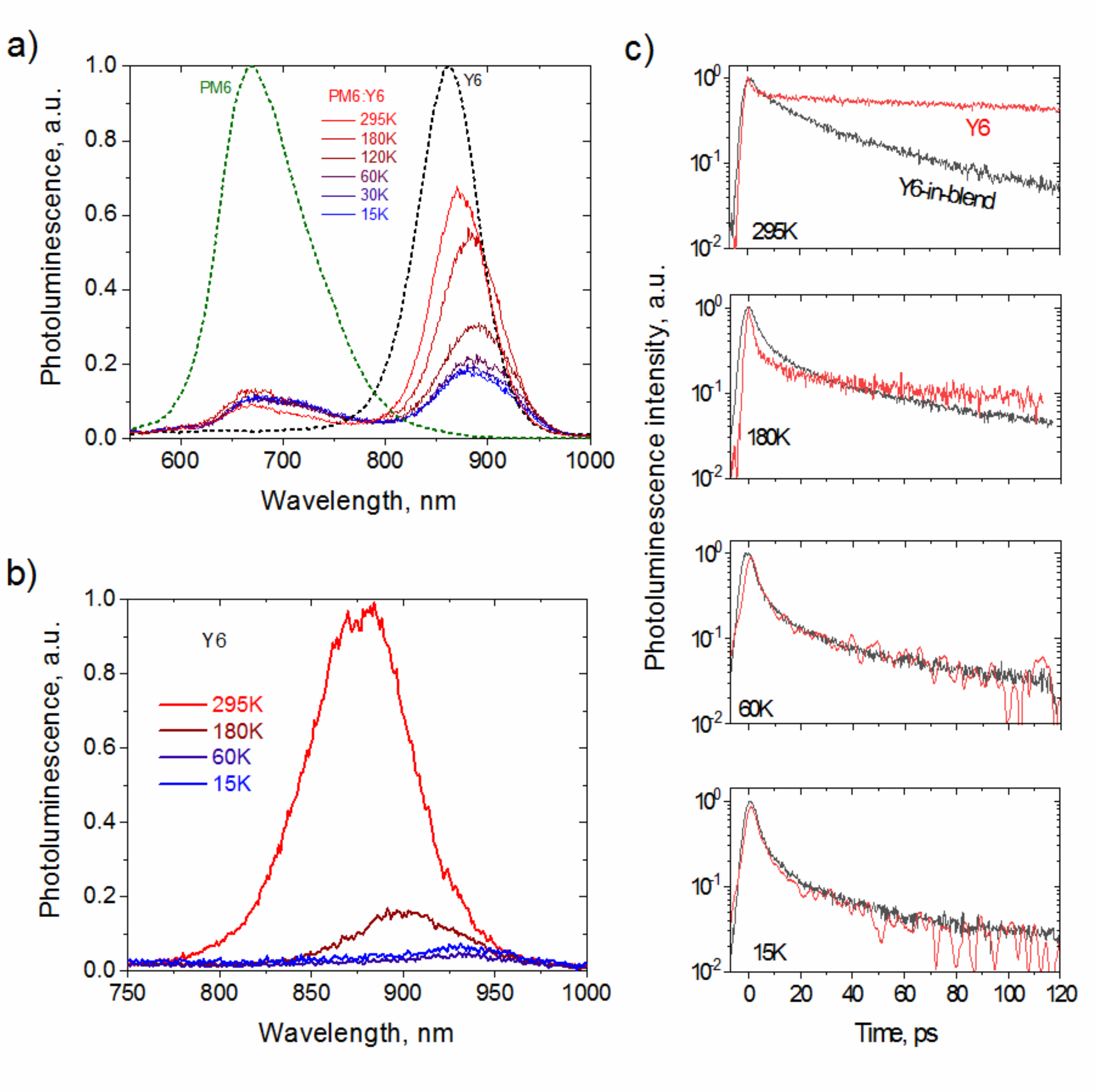

Figure 4. *Temporally integrated (0-120ps) photoluminescence spectra of PM6:Y6 blend (a) and Y6 film (b) at various temperatures after excitation with a 515nm laser pulse. The green and black dashed curves in (a) indicate the photoluminescence spectra of the neat PM6 and Y6 films; c) Y6 and Y6-in-blend photoluminescence kinetics at various temperatures.*

In contrast, the PL intensity of the acceptor is much stronger and decreases sharply with temperature. Zhu et al. have recently demonstrated that the photoluminescence intensity of pure Y6 film also decreases at lower temperatures[38]. This unconventional behavior was explained by the assumption that strong polarization effects reduce the energy of the charge-separated state (xCT) even below that of the lowest excited singlet state, resulting in effective charge separation within the Y6 material. The fluorescence of Y6 is attributed to thermal repopulation of the A* state - a kind of thermally activated luminescence (TAL) with an activation energy of ~185 meV, which is easily overcome at room temperature, but strongly hinders exciton reforming and thus luminescence at lower temperatures. We observe a similar trend in blend, where PL intensity decreases about threefold when the temperature is reduced from RT to 60 K (see Fig. 4a), and remains stable at lower temperatures. However, this decrease is much weaker than the approximately 20-fold PL decrease in the pure Y6 film (Fig. 4b).

Figure 4c compares the normalized PL kinetics of the neat Y6 film and the PM6:Y6 blend. In both cases, the PL kinetics are identical and show a monotonic, non-exponential decay at 15 and 60K. This behavior indicates that the PL decay kinetics are determined solely by intramolecular processes – the barrierless formation of non-fluorescent xCT states. This agrees well with the TA kinetics of the blend under excitation of the acceptor, which shows that only the ultrafast PM6 bleaching component caused by hole transfer from the "hot" **A*** state remains at very low temperatures. Thus, there is neither hole transfer to the donor nor **A*** quenching at longer times addressed by tPL measurements. The non-exponential PL decay at these low temperatures is apparently caused by the inhomogeneity of the system: different individual **A** molecules experience different transition rates to the xCT state due to different conformations and environmental influences. At higher temperatures, the PL kinetics of the pure Y6 film clearly shows two decay components: the fast component related to the formation of the xCT state and a slow TAL component whose intensity increases with temperature. Some decrease in TAL intensity during 120 ps gives a lifetime of the combined A*/xCT state of about 400 ps, which is similar to but slightly longer than that determined from the TA kinetics of the neat Y6 film. We cannot exclude that the TA decay is influenced by exciton-exciton annihilation, which causes a faster decay.

PL kinetics of the blend undergo less significant changes with temperature than that of pure Y6. However, the fast decay component becomes less expressed at higher temperatures, while the slow component becomes slightly faster (a more detailed temperature dependence showing these changes more clearly is presented in SI Fig. S5). These changes are apparently governed by the competition between the thermal reactivation of the **A*** state and the hole transfer to the donor material. Hole transfer shortens the lifetime of the xCT state and the TAL, leading to a faster PL decay of the blend compared to pure Y6. The rate of the hole transfer apparently decreases at low temperatures and ceases completely at 60k. The competition of this process with the recreation of the A* state, which is also temperature dependent, causes a less significant temperature dependence of the blends PL intensity compared to pure Y6.

3. Carrier generation and recombination model

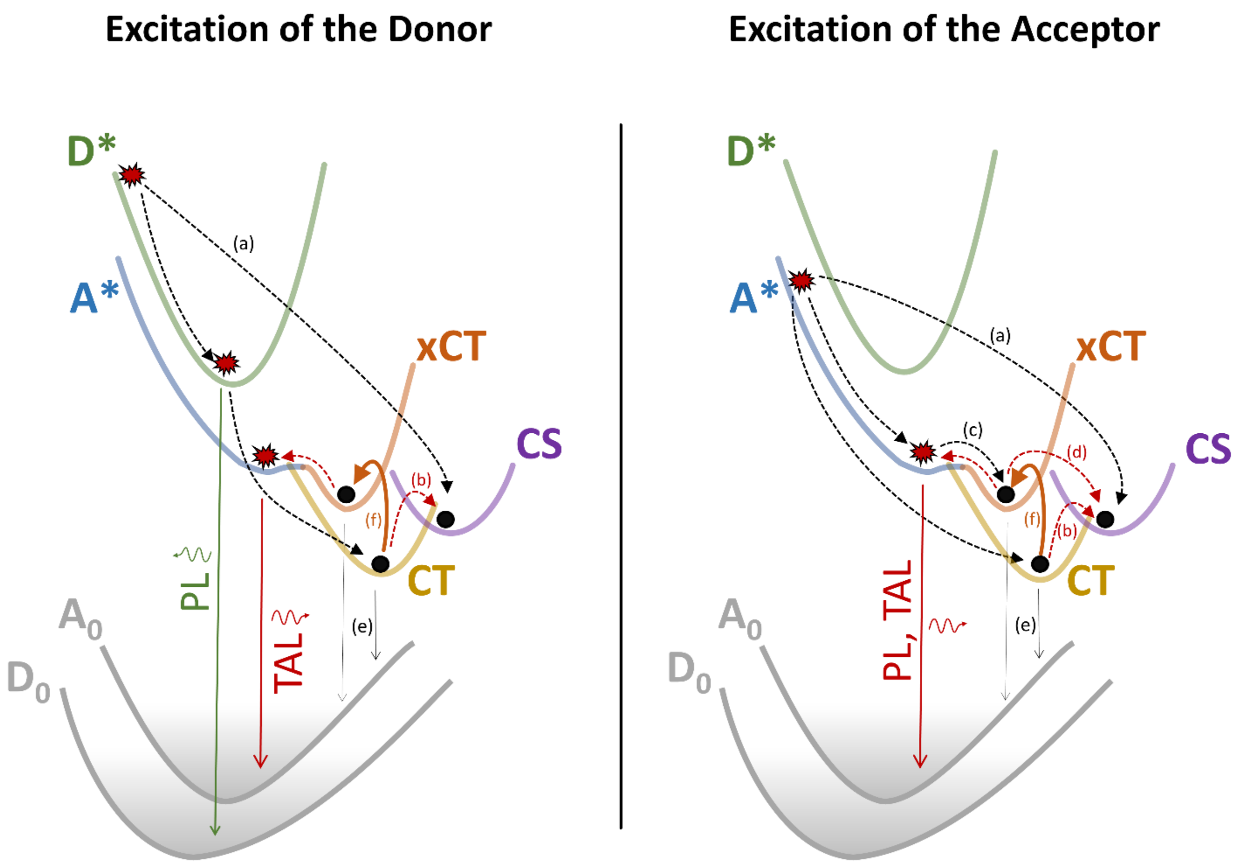

Figure 5. *Schematic representation. Explanation in the text.*

The schematics shown in Figure 5 summarize the experimental data and show the main electronic processes that occur in the solar cell during the first few nanoseconds under excitation of the donor and acceptor. Black arrows show processes that do not require thermal activation, while red arrows show thermally activated processes. As it is shown, the formation of the CT states does not require thermal assistance under either donor or acceptor excitation. Moreover, some of the **D*** (or **A***) states that are not yet in equilibrium form CS even without thermal assistance in a time scale of less than one picosecond (denoted as (a)). In contrast, the formation of the CS states from equilibrated CT states requires thermal assistance and stops almost completely at 60 K (b). Excitation of the acceptor also leads to additional, temperature-independent formation of the xCT state during a few ps (c). However, the subsequent formation of CS states requires thermal assistance (d). Consequently, the generation of free charge carriers occurs by a temperature-independent process from non-equilibrated **D*** and **A*** states (a) and by thermally activated separation of CT (b) and xCT (d) states. The solid black arrows show the non-radiative recombination pathways (e). The partial recovery of the acceptor absorption on an ns time scale at temperatures below 180 K, when the reformation of **A*** and the formation of the CT state do not occur (see Figures 2 and 3), indicates the presence of a temperature-independent relaxation channel of the xCT state to the acceptor ground state. This is a loss channel, but is less efficient at higher temperatures when the formation of the CT state and the reformation of the **A*** state are present. The xCT state is also subject to recombination through the reformation of the **A*** state. This pathway is represented by the TAL. However, the TAL signal decays much faster in the blend at room temperature than in the pure Y6 film, so this loss channel is obviously not significant.

The thick dark orange curves (f) show the reverse electron transfer to the donor (or hole transfer to the acceptor) opened by a small HOMO level offset that reopens the e-h recombination pathway in the acceptor and creates an additional channel for the solar cell efficiency loss.

4. Conclusions

In this work we have investigated the mechanism of charge carrier generation in PM6:Y6 bulk heterojunctions using transient absorption and transient photoluminescence at temperatures ranging from 295 K down to 15 K. There are different pathways of charge carrier generation and recombination that depend on either excitation of the donor or acceptor. When the donor is photoexcited, the generation of interfacial CT excitons is almost temperature-independent, while their separation into free charge carriers is highly suspended at low temperatures and dominated by ultrafast separation from non-equilibrated interfacial CT state. When an acceptor is excited, charge carrier generation occurs via two different pathways: the interfacial CT state and the intra-moiety xCT state, and both pathways contribute about equally at room temperature. The conventional pathway is almost temperature independent, whereas charge carrier generation via the xCT state requires thermal assistance. Charge carrier recombination also occurs via thermally independent recombination of interfacial CT and xCT states, and via thermally activated reverse electron transfer from the acceptor to the donor, which is related to the small HOMO level offset and restores the singlet exciton state of the acceptor. The latter channel is the most significant at room temperature and causes a loss of charge carrier generation efficiency of more than 10%. Consequently, a small energy offset between the HOMO levels of donor and acceptor opens an additional loss channel. This relaxation pathway requires a subtle balance between minimizing the HOMO level offset, which increases V_{OC} but causes current losses due to reverse electron transfer.

Supporting Information

Supporting Information is available from the Wiley Online Library or from the author.

Received: ((will be filled in by the editorial staff))
Revised: ((will be filled in by the editorial staff))
Published online: ((will be filled in by the editorial staff))

References

(1) Inganäs, O. Organic Photovoltaics over Three Decades. *Advanced Materials* **2018**, *30* (35), 1800388. https://doi.org/10.1002/adma.201800388.

(2) Qi, F.; Jiang, K.; Lin, F.; Wu, Z.; Zhang, H.; Gao, W.; Li, Y.; Cai, Z.; Woo, H. Y.; Zhu, Z.; Jen, A. K.-Y. Over 17% Efficiency Binary Organic Solar Cells with Photoresponses Reaching 1000 Nm Enabled by Selenophene-Fused Nonfullerene Acceptors. *ACS Energy Lett.* **2021**, *6* (1), 9–15. https://doi.org/10.1021/acsenergylett.0c02230.

(3) Liu, L.; Kan, Y.; Gao, K.; Wang, J.; Zhao, M.; Chen, H.; Zhao, C.; Jiu, T.; Jen, A. -Y.; Li, Y. Graphdiyne Derivative as Multifunctional Solid Additive in Binary Organic Solar Cells with 17.3% Efficiency and High Reproductivity. *Adv. Mater.* **2020**, *32* (11), 1907604. https://doi.org/10.1002/adma.201907604.

(4) Ma, R.; Liu, T.; Luo, Z.; Guo, Q.; Xiao, Y.; Chen, Y.; Li, X.; Luo, S.; Lu, X.; Zhang, M.; Li, Y.; Yan, H. Improving Open-Circuit Voltage by a Chlorinated Polymer Donor Endows Binary Organic Solar Cells Efficiencies over 17%. *Sci. China Chem.* **2020**, *63* (3), 325–330. https://doi.org/10.1007/s11426-019-9669-3.

(5) Fan, B.; Zhang, D.; Li, M.; Zhong, W.; Zeng, Z.; Ying, L.; Huang, F.; Cao, Y. Achieving over 16% Efficiency for Single-Junction Organic Solar Cells. *Sci. China Chem.* **2019**, *62* (6), 746–752. https://doi.org/10.1007/s11426-019-9457-5.

(6) He, Q.; Shahid, M.; Wu, J.; Jiao, X.; Eisner, F. D.; Hodsden, T.; Fei, Z.; Anthopoulos, T. D.; McNeill, C. R.; Durrant, J. R.; Heeney, M. Fused Cyclopentadithienothiophene Acceptor Enables Ultrahigh Short-Circuit Current and High Efficiency >11% in As-Cast Organic Solar Cells. *Adv. Funct. Mater.* **2019**, *29* (40), 1904956. https://doi.org/10.1002/adfm.201904956.

(7) Zheng, Z.; Wang, R.; Yao, H.; Xie, S.; Zhang, Y.; Hou, J.; Zhou, H.; Tang, Z. Polyamino Acid Interlayer Facilitates Electron Extraction in Narrow Band Gap Fullerene-Free Organic Solar Cells with an Outstanding Short-Circuit Current. *Nano Energy* **2018**, *50*, 169–175. https://doi.org/10.1016/j.nanoen.2018.05.034.

(8) Cai, F.; Peng, H.; Chen, H.; Yuan, J.; Hai, J.; Lau, T.-K.; Wang, J.; Hu, Y.; Liu, W.; Lu, X.; Zou, Y. An Asymmetric Small Molecule Acceptor for Organic Solar Cells with a Short Circuit Current Density over 24 MA Cm $^{-2}$. *J. Mater. Chem. A* **2020**, *8* (31), 15984–15991. https://doi.org/10.1039/D0TA01636E.

(9) Kan, B.; Zhang, J.; Liu, F.; Wan, X.; Li, C.; Ke, X.; Wang, Y.; Feng, H.; Zhang, Y.; Long, G.; Friend, R. H.; Bakulin, A. A.; Chen, Y. Fine-Tuning the Energy Levels of a Nonfullerene Small-Molecule Acceptor to Achieve a High Short-Circuit Current and a Power

Conversion Efficiency over 12% in Organic Solar Cells. *Advanced Materials* **2018**, *30* (3), 1704904. https://doi.org/10.1002/adma.201704904.

(10) Eisner, F. D.; Azzouzi, M.; Fei, Z.; Hou, X.; Anthopoulos, T. D.; Dennis, T. J. S.; Heeney, M.; Nelson, J. Hybridization of Local Exciton and Charge-Transfer States Reduces Nonradiative Voltage Losses in Organic Solar Cells. *J. Am. Chem. Soc.* **2019**, *141* (15), 6362–6374. https://doi.org/10.1021/jacs.9b01465.

(11) Liu, X.; Du, X.; Wang, J.; Duan, C.; Tang, X.; Heumueller, T.; Liu, G.; Li, Y.; Wang, Z.; Wang, J.; Liu, F.; Li, N.; Brabec, C. J.; Huang, F.; Cao, Y. Efficient Organic Solar Cells with Extremely High Open-Circuit Voltages and Low Voltage Losses by Suppressing Nonradiative Recombination Losses. *Adv. Energy Mater.* **2018**, *8* (26), 1801699. https://doi.org/10.1002/aenm.201801699.

(12) Yang, D.; Wang, Y.; Sano, T.; Gao, F.; Sasabe, H.; Kido, J. A Minimal Non-Radiative Recombination Loss for Efficient Non-Fullerene All-Small-Molecule Organic Solar Cells with a Low Energy Loss of 0.54 EV and High Open-Circuit Voltage of 1.15 V. *Journal of Materials Chemistry A* **2018**, *6* (28), 13918–13924. https://doi.org/10.1039/C8TA04665D.

(13) Classen, A.; Chochos, C. L.; Lüer, L.; Gregoriou, V. G.; Wortmann, J.; Osvet, A.; Forberich, K.; McCulloch, I.; Heumüller, T.; Brabec, C. J. The Role of Exciton Lifetime for Charge Generation in Organic Solar Cells at Negligible Energy-Level Offsets. *Nat Energy* **2020**. https://doi.org/10.1038/s41560-020-00684-7.

(14) Yuan, J.; Zhang, Y.; Zhou, L.; Zhang, G.; Yip, H.-L.; Lau, T.-K.; Lu, X.; Zhu, C.; Peng, H.; Johnson, P. A.; Leclerc, M.; Cao, Y.; Ulanski, J.; Li, Y.; Zou, Y. Single-Junction Organic Solar Cell with over 15% Efficiency Using Fused-Ring Acceptor with Electron-Deficient Core. *Joule* **2019**, *3* (4), 1140–1151. https://doi.org/10.1016/j.joule.2019.01.004.

(15) Yan, T.; Song, W.; Huang, J.; Peng, R.; Huang, L.; Ge, Z. 16.67% Rigid and 14.06% Flexible Organic Solar Cells Enabled by Ternary Heterojunction Strategy. *Adv. Mater.* **2019**, *31* (39), 1902210. https://doi.org/10.1002/adma.201902210.

(16) Ma, Q.; Jia, Z.; Meng, L.; Zhang, J.; Zhang, H.; Huang, W.; Yuan, J.; Gao, F.; Wan, Y.; Zhang, Z.; Li, Y. Promoting Charge Separation Resulting in Ternary Organic Solar Cells Efficiency over 17.5%. *Nano Energy* **2020**, *78*, 105272. https://doi.org/10.1016/j.nanoen.2020.105272.

(17) Distler, A.; Brabec, C. J.; Egelhaaf, H. Organic Photovoltaic Modules with New World Record Efficiencies. *Prog Photovolt Res Appl* **2021**, *29* (1), 24–31. https://doi.org/10.1002/pip.3336.

(18) Wen, Z.-C.; Yin, H.; Hao, X.-T. Recent Progress of PM6:Y6-Based High Efficiency Organic Solar Cells. *Surfaces and Interfaces* **2021**, *23*, 100921. https://doi.org/10.1016/j.surfin.2020.100921.

(19) Guo, Q.; Guo, Q.; Geng, Y.; Tang, A.; Zhang, M.; Du, M.; Sun, X.; Zhou, E. Recent Advances in PM6:Y6-Based Organic Solar Cells. *Mater. Chem. Front.* **2021**, *5* (8), 3257–3280. https://doi.org/10.1039/D1QM00060H.

(20) Yu, R.; Wu, G.; Tan, Z. Realization of High Performance for PM6:Y6 Based Organic Photovoltaic Cells. *Journal of Energy Chemistry* **2021**, *61*, 29–46. https://doi.org/10.1016/j.jechem.2021.01.027.

(21) Wang, R.; Zhang, C.; Li, Q.; Zhang, Z.; Wang, X.; Xiao, M. Charge Separation from an Intra-Moiety Intermediate State in the High-Performance PM6:Y6 Organic Photovoltaic Blend. *J. Am. Chem. Soc.* **2020**, *142* (29), 12751–12759. https://doi.org/10.1021/jacs.0c04890.

(22) Perdigón-Toro, L.; Zhang, H.; Markina, A.; Yuan, J.; Hosseini, S. M.; Wolff, C. M.; Zuo, G.; Stolterfoht, M.; Zou, Y.; Gao, F.; Andrienko, D.; Shoaee, S.; Neher, D. Barrierless Free Charge Generation in the High-Performance PM6:Y6 Bulk Heterojunction Non-Fullerene Solar Cell. *Adv. Mater.* **2020**, *32* (9), 1906763. https://doi.org/10.1002/adma.201906763.

(23) Devižis, A.; Serbenta, A.; Meerholz, K.; Hertel, D.; Gulbinas, V. Ultrafast Dynamics of Carrier Mobility in a Conjugated Polymer Probed at Molecular and Microscopic Length Scales. *Phys. Rev. Lett.* **2009**, *103* (2), 027404. https://doi.org/10.1103/PhysRevLett.103.027404.

(24) Tamura, H.; Burghardt, I. Ultrafast Charge Separation in Organic Photovoltaics Enhanced by Charge Delocalization and Vibronically Hot Exciton Dissociation. *J. Am. Chem. Soc.* **2013**, *135* (44), 16364–16367. https://doi.org/10.1021/ja4093874.

(25) Gélinas, S.; Rao, A.; Kumar, A.; Smith, S. L.; Chin, A. W.; Clark, J. Ultrafast Long-Range Charge Separation in Organic Semiconductor Photovoltaic Diodes. **2014**, *343*, 6.

(26) Abramavicius, V.; Pranculis, V.; Melianas, A.; Inganäs, O.; Gulbinas, V.; Abramavicius, D. Role of Coherence and Delocalization in Photo-Induced Electron Transfer at Organic Interfaces. *Sci Rep* **2016**, *6* (1), 32914. https://doi.org/10.1038/srep32914.

(27) Chen, S.; Myeon Lee, S.; Xu, J.; Lee, J.; Cheol Lee, K.; Hou, T.; Yang, Y.; Jeong, M.; Lee, B.; Cho, Y.; Jung, S.; Oh, J.; Zhang, Z.-G.; Zhang, C.; Xiao, M.; Li, Y.; Yang, C. Ultrafast Channel II Process Induced by a 3-D Texture with Enhanced Acceptor Order Ranges for High-Performance Non-Fullerene Polymer Solar Cells. *Energy & Environmental Science* **2018**, *11* (9), 2569–2580. https://doi.org/10.1039/C8EE01546E.

(28) Franco, V. A. C.; Gasparini, N.; Nagahara, T.; Lüer, L.; Cerullo, G.; Brabec, C. Instantaneous Charge Separation in Non-Fullerene Acceptor Bulk-Heterojunction of Highly

Efficient Solar Cells. *EPJ Web Conf.* **2019**, *205*, 05010. https://doi.org/10.1051/epjconf/201920505010.

(29) Stoltzfus, D. M.; Donaghey, J. E.; Armin, A.; Shaw, P. E.; Burn, P. L.; Meredith, P. Charge Generation Pathways in Organic Solar Cells: Assessing the Contribution from the Electron Acceptor. *Chemical Reviews* **2016**, *116* (21), 12920–12955. https://doi.org/10.1021/acs.chemrev.6b00126.

(30) Gasparini, N.; Wadsworth, A.; Moser, M.; Baran, D.; McCulloch, I.; Brabec, C. J. The Physics of Small Molecule Acceptors for Efficient and Stable Bulk Heterojunction Solar Cells. *Advanced Energy Materials* **2018**, *8* (12), 1703298. https://doi.org/10.1002/aenm.201703298.

(31) Mikhnenko, O. V.; Cordella, F.; Sieval, A. B.; Hummelen, J. C.; Blom, P. W. M.; Loi, M. A. Temperature Dependence of Exciton Diffusion in Conjugated Polymers. *J. Phys. Chem. B* **2008**, *112* (37), 11601–11604. https://doi.org/10.1021/jp8042363.

(32) Tamai, Y.; Fan, Y.; Kim, V. O.; Ziabrev, K.; Rao, A.; Barlow, S.; Marder, S. R.; Friend, R. H.; Menke, S. M. Ultrafast Long-Range Charge Separation in Nonfullerene Organic Solar Cells. *ACS Nano* **2017**, *11* (12), 12473–12481. https://doi.org/10.1021/acsnano.7b06575.

(33) Chen, K.; Barker, A. J.; Reish, M. E.; Gordon, K. C.; Hodgkiss, J. M. Broadband Ultrafast Photoluminescence Spectroscopy Resolves Charge Photogeneration via Delocalized Hot Excitons in Polymer:Fullerene Photovoltaic Blends. *J. Am. Chem. Soc.* **2013**, *135* (49), 18502–18512. https://doi.org/10.1021/ja408235h.

(34) Dimitrov, S. D.; Bakulin, A. A.; Nielsen, C. B.; Schroeder, B. C.; Du, J.; Bronstein, H.; McCulloch, I.; Friend, R. H.; Durrant, J. R. On the Energetic Dependence of Charge Separation in Low-Band-Gap Polymer/Fullerene Blends. *J. Am. Chem. Soc.* **2012**, *134* (44), 18189–18192. https://doi.org/10.1021/ja308177d.

(35) Devizis, A.; Meerholz, K.; Hertel, D.; Gulbinas, V. Ultrafast Charge Carrier Mobility Dynamics in Poly(Spirobifluorene- c o -Benzothiadiazole): Influence of Temperature on Initial Transport. *Phys. Rev. B* **2010**, *82* (15), 155204. https://doi.org/10.1103/PhysRevB.82.155204.

(36) Grancini, G.; Maiuri, M.; Fazzi, D.; Petrozza, A.; Egelhaaf, H.-J.; Brida, D.; Cerullo, G.; Lanzani, G. Hot Exciton Dissociation in Polymer Solar Cells. *Nature Materials* **2013**, *12* (1), 29–33. https://doi.org/10.1038/nmat3502.

(37) Perdigón-Toro, L.; Phuong, L. Q.; Zeiske, S.; Vandewal, K.; Armin, A.; Shoaee, S.; Neher, D. Excitons Dominate the Emission from PM6:Y6 Solar Cells, but This Does Not Help the Open-Circuit Voltage of the Device. *ACS Energy Lett.* **2021**, *6* (2), 557–564. https://doi.org/10.1021/acsenergylett.0c02572.

(38) Zhu, L.; Zhang, J.; Guo, Y.; Yang, C.; Yi, Y.; Wei, Z. Small Exciton Binding Energies Enabling Direct Charge Photogeneration Towards Low-Driving-Force Organic Solar Cells. *Angew. Chem. Int. Ed.* **2021**, *60* (28), 15348–15353. https://doi.org/10.1002/anie.202105156.

Combined transient absorption and time resolved photoluminescence studies revealed several parallel charge carrier generation pathways, which determine performance efficiency of non-fullerene PM6/Y6 organic solar cell. Small offset between donor and acceptor HOMO levels enables high V_{oc}, yet opens a thermally activated recombination loss channel by reverse electron transfer from acceptor to donor.

Rokas Jasiūnas, Huotian Zhang, Andrius Devižis, Marius Franckevičius, Feng Gao and Vidmantas Gulbinas*

Thermally activated reverse electron transfer limits carrier generation efficiency in PM6:Y6 non-fullerene organic solar cells

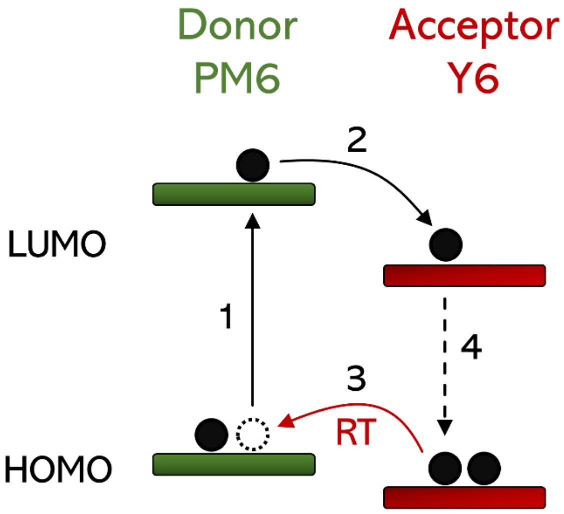

ToC Figure

Supporting Information

Thermally activated reverse electron transfer limits carrier generation efficiency in PM6:Y6 non-fullerene organic solar cells

Rokas Jasiūnas, Huotian Zhang, Andrius Devižis, Marius Franckevičius, Feng Gao and Vidmantas Gulbinas*

MATERIALS AND METHODS

Sample Preparation.

Glass substrates with patterned indium tin oxide electrodes were cleaned were cleaned by water-detergent mixture for 20-min in ultrasonic cleaner, then rinsed by deionized water for more than five times. Subsequently, the substrates were transferred into acetone and isopropanol for 20-min ultrasonic cleaning, respectively. After the cleaning, substrates were dried by nitrogen and applied with 10-min ultraviolet-ozone treatment. A layer of poly(3,4-ethylenedioxythiophene)-poly(styrenesulfonate) (PEDOT:PSS, 4083, purchased from Heraeus) was spin-coated on the substrate with 4000 rpm, and then annealed at 150 °C for 10 min. The substrates with PEDOT:PSS were transferred into a nitrogen glovebox for active layer spin-coating. PM6 and Y6 (purchased from Solarmer Materials Inc (Beijing)) were dissolved in chloroform (CF) to a total concentration of 16 mg/mL for 2 h, with a 1 to 1.2 weight ratio, and 0.5% 1-chloronaphthalene (v:v, CN:CF) as an additive. The solution was spin-coated with 4000 rpm and then annealed at 150 °C for 10 min. Poly(9,9-bis(3'-(N,N-dimethyl)-N-ethylammoinium-propyl-2,7-fluorene)-alt-2,7-(9,9-dioctylfluorene))dibromide (PFN-Br) dissolved in methanol (0.5 mg/ml) was spin-coated with 3500 rpm. Finally, the substrates were transported into a vacuum chamber for metal electrode evaporation. A layer of 100 nm Al was evaporated through a shadow mask in a vacuum of 10^{-6} mbar.

Transient Absorption Spectroscopy.

The transient absorption setup was based on the amplified femtosecond laser Pharos 10-600-PP laser (Light Conversion Ltd.), operating at fundamental wavelength of 1032 nm, repetition rate of 200 kHz, and pulse width of <250 fs. The measurements were performed at repetition rate of 200/42 = 4.762 kHz frequency achieved by using the pulse picker. The collinear optical parametric amplifier Orpheus PO15F2L (Light Conversion Ltd.) was used to obtain 560 nm or 820nm wavelength pulses for sample excitation. Excitation was modulated at 4.762/6 = 0.794 kHz frequency by mechanical chopper synchronized to the output of the pulse picker. As a probe, pulses were used, spectrally broadened by means of continuum generation in the sapphire crystal. The detection equipment consisted of Andor-Shamrock SR-500i-B1-R spectrometer (Andor Technology, 150 lines mm−1 diffraction grating) equipped with Andor-Newton (Andor Technology) DU970 CCD camera (1600 × 200 pixels). The reading of the camera was synchronized with the chopper.

Electroabsorption

Experimental method is based on the measurement of the electric field-induced absorption changes (Stark effect) of organic films sandwiched between semitransparent and metal electrodes. Under reverse bias, when equilibrium carriers are extracted from the active media and their injection is negligible, the material between electrodes behaves like a dielectric medium, and the device resembles a charged capacitor. Under these conditions the applied external bias results in the homogeneously distributed electric field inside the organic layer.

For EA measurements we used the same femtosecond absorption pump−probe spectrometer as for transient absorption, extended with square voltage generator and oscilloscope. The p-polarized white light generated in a sapphire plate was used for probing EA of the samples in reflection configuration at 45 degrees of the incidence angle. Square voltage pulses of reverse bias, synchronized to the laser output and having a duration of about 100 μs were applied to the sample by means of an electrical pulse generator at a frequency of 500 Hz. The measured electroabsorption corresponded to the absorption difference between the biased and unbiased sample at a given probe pulse delay. An oscilloscope was used to measure the photocurrent through a 50 Ω load.

UV-Vis absorption.

UV-Vis absorption spectra were recorded with a Jasco V-670 spectrophotometer in the range of 300-900 nm.

Transient Photoluminescence.

Time-resolved PL investigations were performed by means of Hamamatsu Streak camera operating in a single sweep regime. Femtosecond Yb:KGW laser (Light Conversion Ltd.) producing 80 fs, 1030 nm light pulses at a repetition rate of 76 MHz was employed for the sample excitation. Third harmonics beam of the femtosecond laser (345 nm) (generated by HIRO harmonics generator, Light Conversion Ltd.) used for excitation was focused into a ≈30 µm spot on the sample. Excitation power density was attenuated using neutral density filters to ≈250 mW cm−2. The time resolution of the entire system was ≈13 ps.

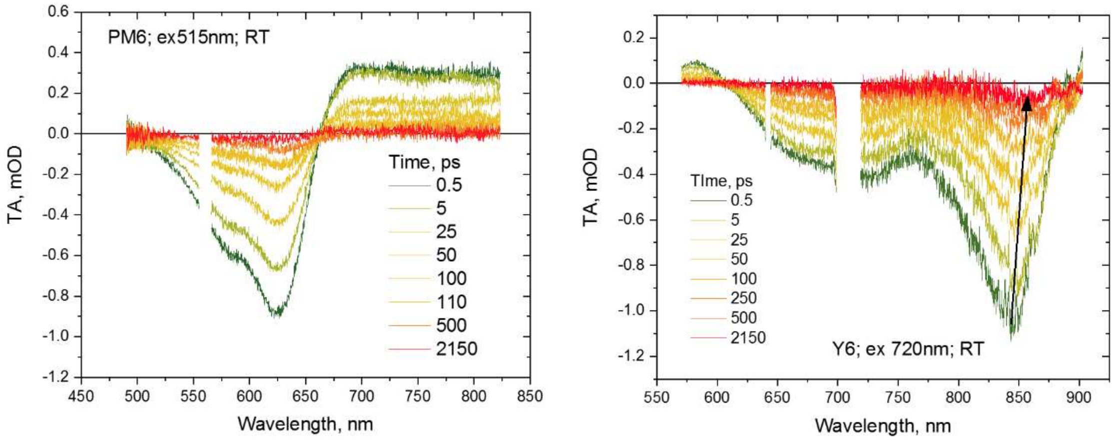

Figure S1. *Time evolution of transient absorption spectra of neat PM6 and Y6 films, after 515nm and 720nm excitation, respectively.*

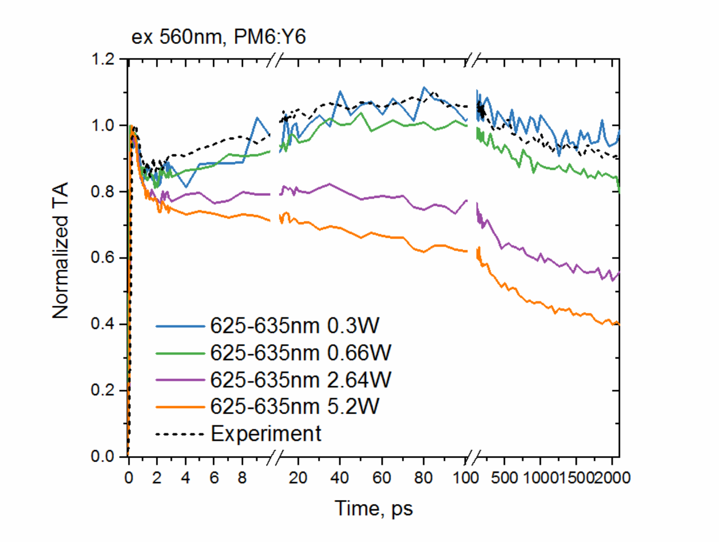

Figure S2. *TA intensity dependence measured under excitation of donor at RT. Experiment indicates kinetics obtained at intensities used in investigations described in the main text. At high excitation intensities the decay rates increase due to nongeminate carrier recombination.*

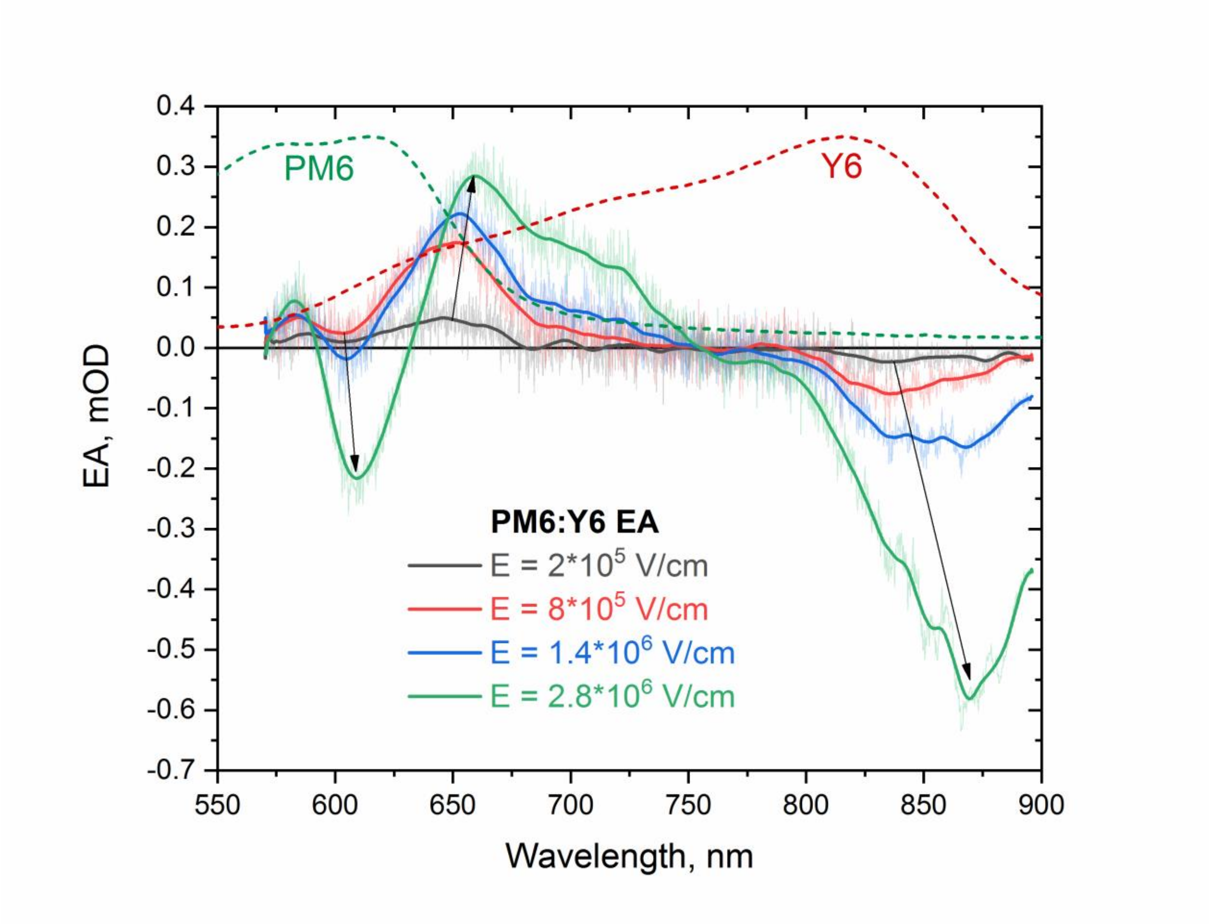

Figure S3. *Electroabsorption spectra of the PM6:Y6 blend at different applied voltages Uapp values. Dotted curves indicate normalized steady state absorption of neat PM6 and Y6 films.*

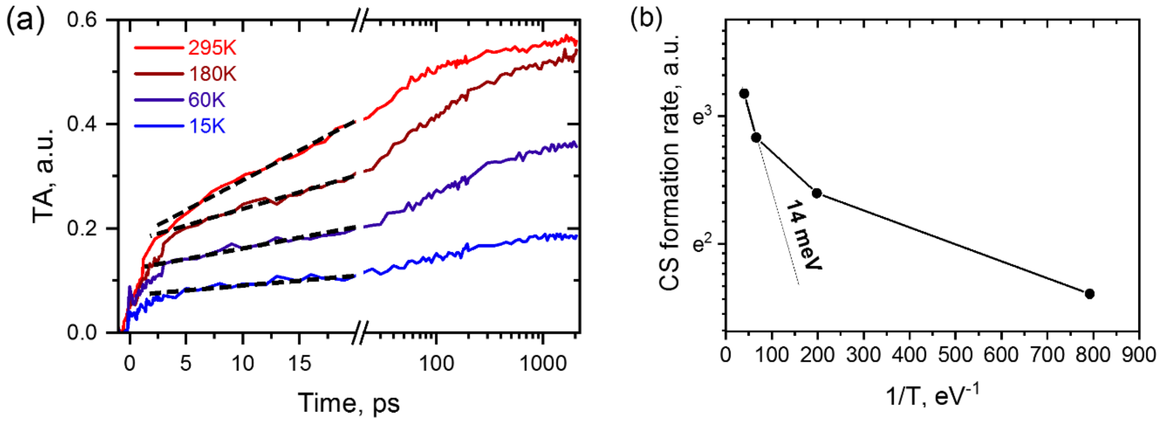

Figure S4. (a) *Kinetics of the induced absorption in the 750-775 nm region attributed to CS states. Black dashed lines show formation rates of CS states in 2-20 ps time interval. (b) Arrhenius Plot obtained from the CS state formation rates approximated by dashed lines in (a).*

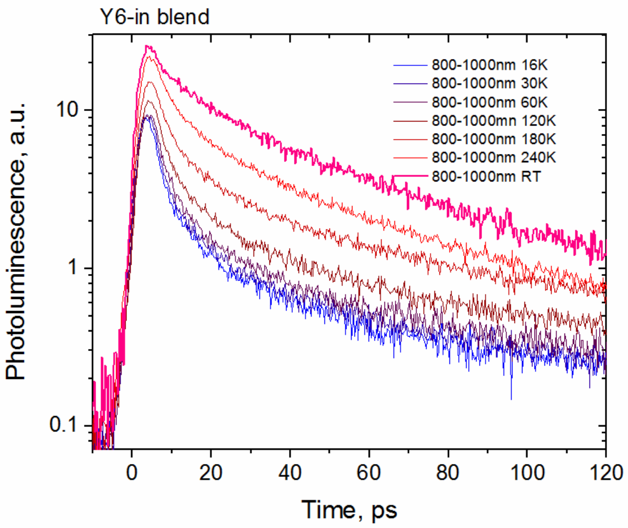

Figure S5. *Transient photoluminescence intensity kinetics of Y6 in PM6:Y6 blend at various temperatures.*